

Models of gravitational lens candidates from Space Warps CFHTLS

Rafael Küng,¹ Prasenjit Saha,¹ Ignacio Ferreras,² Elisabeth Baeten,³ Jonathan Coles,⁴ Claude Cornen,³ Christine Macmillan,³ Phil Marshall,⁵ Anupreeta More,⁶ Lucy Oswald⁷ Aprajita Verma⁸ and Julianne K. Wilcox³

¹Physik-Institut, University of Zurich, Winterthurerstrasse 190, 8057 Zurich, Switzerland

²Mullard Space Science Laboratory, University College London, Holmbury St Mary, Dorking, Surrey RH5 6NT, UK

³Zooniverse, c/o Astrophysics Department, University of Oxford, Oxford OX1 3RH, UK

⁴Physik-Department, Technische Universität München James-Franck-Str. 1, 85748 Garching, Germany

⁵Kavli Institute for Particle Astrophysics and Cosmology, Stanford University, 452 Lomita Mall, Stanford, CA 94035, USA

⁶Kavli IPMU (WPI), UTIAS, University of Tokyo, Kashiwa, Chiba 277-8583, Japan

⁷Murray Edwards College, University of Cambridge, Cambridge CB3 0DF, UK

⁸Sub-department of Astrophysics, University of Oxford, Denys Wilkinson Building, Keble Road, Oxford, OX1 3RH, UK

Accepted XXX. Received YYY; in original form ZZZ

ABSTRACT

We report modelling follow-up of recently-discovered gravitational-lens candidates in the Canada France Hawaii Telescope Legacy Survey. Lens modelling was done by a small group of specially-interested volunteers from the Space Warps citizen-science community who originally found the candidate lenses. Models are categorised according to seven diagnostics indicating (a) the image morphology and how clear or indistinct it is, (b) whether the mass map and synthetic lensed image appear to be plausible, and (c) how the lens-model mass compares with ~~compares with the stellar mass and the abundance-matched halo mass derived from photometry of the lensing galaxy.~~

~~The lens model~~. The lensing masses range from $\sim 10^{11} M_{\odot}$ to $> 10^{13} M_{\odot}$. Preliminary estimates of the stellar masses show ~~(with two outliers)~~ a smaller spread in stellar mass ~~(except for two lenses)~~; a factor of a few below or above $\sim 10^{11} M_{\odot}$. ~~That is, the stellar-mass fraction declines sharply as total~~ Therefore, we expect the stellar-to-total mass fraction to decline sharply as lensing mass increases. The ~~highest mass~~ most massive system with a convincing model is J1434+522 (~~SW05~~SW 05). The two low-mass outliers are J0206-095 (~~SW19~~SW 19) and J2217+015 (~~SW42~~SW 42); if these two are indeed lenses, they ~~are probing~~ probe an interesting regime of very low star-formation efficiency.

Some improvements to the modelling software ~~used~~ (SpaghettiLens), and discussion of strategies ~~for regarding~~ scaling to future surveys with more and frequent discoveries, are ~~also~~ included.

Key words: gravitational lensing: strong – galaxies: general – ~~galaxies: stellar content~~ – ~~dark matter~~.

1 INTRODUCTION

By ~~a curious~~ coincidence, the typical escape velocity of massive galaxies ~~– of order a few hundred km/s –~~ is such that v_{esc}^2/c^2 , ~~expressed as an angular distance~~, is comparable to the apparent sizes of ~~a~~-galaxies at cosmological distances. This coincidence is fortunate, because it makes the ~~gravitational~~ lensing deflection angle ~~(which is $2v_{\text{esc}}^2/c^2$)~~ of distant galaxies ~~($\alpha \sim 2v_{\text{esc}}^2/c^2$)~~ comparable to their size on the sky, ~~and as~~. As a result, strong lensing by galaxies ~~tends~~

~~to produce produces~~ images that probe ~~the dark halos of those galaxies. This is important, because while their host dark matter halos, providing a useful tool to understand galaxy formation. While there is a general consensus that basic mechanism of galaxy formation involves about the basic mechanisms at play, involving~~ gravitational collapse, fragmentation, and mergers of dark-matter clumps, into which gas fell, cooling through radiative processes to form dense clouds and eventually stars, there is much debate about

the details (for a summary, see Silk & Mamon 2012). In particular, the nature of dark matter remains mysterious: most researchers take it to be a collisionless non-relativistic fluid (cold dark matter or CDM) readily studied by simulations (for example, the influential millenium simulation by Springel et al. 2005). But other (for example, the influential Millennium simulation, However, alternative scenarios, where dark matter has exotic dynamical properties (Saxton & Ferreras 2010; Schive et al. 2016), or is not really matter at all, but a modification of gravity (McGaugh et al. 2016), have also been considered.

All this motivates using galaxy lenses—the use of strong gravitational lensing over galaxy scales to study the mutual dynamics of dark matter, gas and stars in galaxies. Several studies in recent years have done so (Koopmans et al. 2009; Leier et al. 2011, 2012, 2016; Bruderer et al. 2014; Somerville et al. 2014; Somerville et al. 2017; More et al. 2012; Maturi et al. 2014; Gavazzi et al. 2014) by either machine learning methods (e.g., Paraficz et al. 2016; Lanusse et al. 2017) or visual inspection by citizen-science volunteers in Space Warps through the Space Warps project (More et al. 2016) have, between them, discovered an average of four lenses per square degree, so one can be optimistic about finding many thousands of lenses in the next generation of wide-field surveys, from the LSST in optical and the ground-based surveys such as LSST in the optical window and SKA in radio on the ground, and to space-based missions such as Euclid and WFIRST in orbit.

The expected flood of new lens discoveries will need a similarly huge—large modelling effort to reconstruct their mass distributions. To prepare for the challenge of massive sample lens modelling, Lens-modelling robots have started to be developed (Nightingale et al. 2017; Hezaveh et al. 2017) but so far are able to handle only very clean systems. For typical lenses, human input is still needed. With that in mind Küng et al. (2015) developed a new modelling strategy, implemented as the SpaghettiLens¹ system. The idea is to collaborate with experienced members of the citizen-science community, who have already participated in lens discovery through Space Warps, as well as several other projects involving astronomical data. The system was tested on a sample of simulated lenses, which were part of the training and testing set in Space Warps.

This paper continues follows up that study by applying SpaghettiLens to lens candidates discovered through Space Warps candidates discovered through Space Warps. We present results from modelling the modelling of 58 of 56 of the 59 lens candidates reported by More et al. (2016). Each lens candidate was modelled in following a collaborative refinement process, where anyone interested can create a new model or modify could improve the analysis by modifying

an existing model to try and make it better.² The result or creating a new one. Note the difference with respect to the main Space Warps project, where volunteers from a group of $\gtrsim 10^4$ people make independent contributions. Each person is presented with a random selection of survey-patches and Springel et al. (2005) vote on each. The system estimates the skill level of each volunteer according to test-patches interspersed with the real data, and weights their votes accordingly (Marshall et al. 2016). There is an active forum for volunteers, but since everyone is seeing different data samples with minimal overlap, the forum has little if any influence on the votes. In SpaghettiLens, the number of volunteers is significantly lower, but the level of interaction is higher. The resulting model represents a consensus among contributors as to the best that could be achieved with the available data and software.

We emphasize that the interpretation of the results presented here is tentative, because the systems are lens candidates at this stage, not secure lenses. Moreover the candidate-lens redshifts have large uncertainties, while the candidate-source redshifts can only be guessed at present. Nevertheless it is interesting to explore the trends observed with the already available data.

Somerville et al. 2014; Somerville et al. 2017) organized as follows: Section 2 introduces the candidate lenses, their models and the diagnostics applied to them. The following sections elaborate on the diagnostics. Image morphology diagnostics are explained in Section 3 and diagnostics based on the mass models are discussed in Section 4. Stellar masses are presented in Section 5, to compare stellar and lensing masses. Finally, section 6 summarises and tabulates the diagnostics in Table 1.

We include three appendices devoted to various technical issues relating to the modelling. The online supplement gives the results from all the modelled systems generated for all the lensing candidates.

2 THE CANDIDATES AND MODELS

Space Warps is a citizen science gravitational lens search (Marshall et al. 2016). Its first run searched the CFHT Legacy Survey, a survey carried out in five optical bands (u^*, g^*, r^*, i^*, z^*) covering a total area of 160 deg^2 divided up into four fields W1 – W4. The MegaPrime camera, used for the survey, has a field of view of 1 deg^2 , with $0.186''$ pixels. The flux limit of the survey is $g^* < 25.6 \text{ AB}$ (5σ) with a typical seeing FWHM $\sim 0.7''$ (Erben et al. 2013). The cutouts shown to the volunteers were colour composites of the g^* , r^* and i^* bands from randomly chosen regions. The programme resulted in 59 new lens candidates, of which

² This is in contrast to the main Space Warps project for discovering lenses, where volunteers in a crowd of $\gtrsim 10^4$ make independent contributions. Each person is presented with a random selection of survey-patches and invited to (in effect) vote on each. The system estimates each volunteer's skill level according to test patches interspersed with the real data, and weights their votes accordingly (Marshall et al. 2016). There is an active forum for volunteers, but since everyone is seeing different data samples with minimal overlap, the forum has little if any influence on votes.

¹ <http://labs.spacewarps.org/spaghetti/>

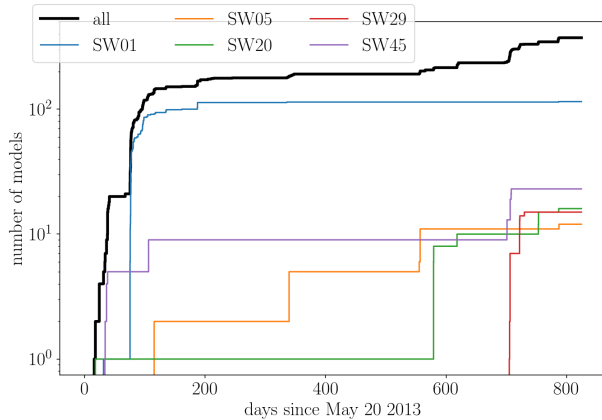


Figure 1. Number of models generated over time in days since the launch of SpaghettiLens; the black line shows all models, the coloured lines show the five most active candidates. A total of 377 models were generated for 58 lens candidates, eight users contributed more than five models per person.

29 are considered high quality. Moreover, 82 previously known lens candidates were “rediscovered”. The candidates have broadly similar redshifts ($0.2 < z < 1.0$), Einstein radii between 0.7 and 5”, and arc fluxes in g -band AB magnitudes between 22 and 26. These properties are similar to those found by previous robotic searches like ArcFinder and RingFinder (More et al. 2016).

A first version of SpaghettiLens was launched in May 2013, while the first run of Space Warps was ongoing. Fig. 1 shows the total number of models generated since launch for our lens candidates. A small number of volunteers started creating models of possible lens candidates from Space Warps that were debated in the discussion forum. In the beginning of August 2013 (around day 70 since release) a modelling challenge for the candidate later to be identified as SW01 was launched. A group of five volunteers presented their results in an online letter converging on a set of 30 models. In April 2015 (day 700), the first major version of SpaghettiLens was released. At the same time, the list of identified candidates was made available (as a preprint of More et al. 2016). At this stage, the volunteers were asked to create models for all the lens candidates that were still missing. The work done for candidate SW29 shows that the volunteers converged on a favourable model much faster, after 15 models, generated in 30 days. The total modelling effort resulted in a set of 377 SpaghettiLens models for all but one of the 59 Space Warps lens candidates; candidate SW39 was not modelled by any volunteer. Over its runtime, the system logged eight major contributors (defined as volunteers that generated, at least, five models).

In parallel, Küng et al. (2015) tested the system on simulated lenses and identified some areas for improvement. In § A1 we introduce fitting of the surface brightness profile of the source. This feature has not been included yet in SpaghettiLens, but we carried the analysis during post-processing for a few interesting cases. In § A2 we show that fine-grained mass maps within the central region relieves a tendency in the earlier work for mass profiles to

be too shallow. In § A3 we consider the possibility of fitting a parametric lens model to the ensemble.

We characterise each model with seven diagnostics, grouped into three categories, whose purpose is to help identify which systems are most probably lenses, and which ones are likely to be most rewarding the most likely cases of a gravitational lens, as well as flag the most interesting candidates for future follow-up observations. The diagnostics are as follows.

- **First** Firstly we have diagnostics based on morphology of the system. Section 3 and Figure Fig. 2 explain this diagnostic in more detail. We consider:

- (i) Whether the images are unblended. **Distinct**: Distinct, unblended images are an advantage in modelling, but although not essential.
- (ii) Whether all images are discernible. The topography of an arrival-time surface, as encoded by a spaghetti diagram, may require more images than are visible, in which case the modeller has to insert conjectural image positions.
- (iii) Whether the lens is fairly isolated.
- (iv) The image morphology concisely described: double or quads, further sub-categorised to indicate the elongation direction of the lensing mass.

- **Second** Secondly we have mass models, covered in Section 4. We assess the following points:

- (v) Whether the mass map is reasonable (see Fig. 5). **Figure 5**
- (vi) Whether the arrival-time surface and synthetic image are plausible. In particular, an unsatisfactory model is flagged when additional images are implied in regions where they are not observed signal an unsatisfactory model. Figures 3 and 4 and 6 (see Figs. 3, 4 6).

- **Third** Thirdly, whether the total implied lensing mass determined from the lens model is plausible, given the photometry of the lensing galaxy. Section 5 explains how we compare. In this work we define the lensing mass as the sum of all mass tiles in the model. These mass tiles reach out to typically twice the radius of the outermost image. Section 5 explains how we compare the lensing (i.e. total) mass with the mass in stars in the lensing galaxy. We estimate the stellar mass by comparing galaxy magnitudes from the CFHTLS pipeline with the well-known stellar-population models of Bruzual & Charlot (2003). We then extrapolate the stellar mass to a halo mass using the abundance-matching prescription of Moster et al. (2010). Naturally, the lensing mass must be more than should be somewhere between the stellar mass but no more than (lower bound) and the total halo mass (upper bound).

- (vii) We then introduce what we call a so-called halo index (H) which gives an idea of that quantifies how the lensing mass compares with these two constraints. **Figure 7**. (see Fig. 7).

Section 6 summarises and tabulates the diagnostics in Table 1. Interpretation of the results is tentative, because the systems are lens candidates at this stage, not secure lenses. Moreover the candidate lens redshifts have large uncertainties, while the candidate source redshifts can only be guessed at present. Nevertheless it is interesting to see

~~what trends we can observe with the already available data.~~

~~There are three appendices devoted to various technical issues relating to modelling. Küng et al. (2015) tested the system on simulated lenses and identified some areas for improvement. In § A1 we introduce fitting of the brightness profiles of the source. This feature has not yet been included in SpaghettiLens, but has been carried out in post-processing for a few especially interesting candidates. In § A2 we show that making mass maps fine-grained in the central region relieves a tendency in the earlier work for mass profile to be too shallow. Then in § A3 we consider the possibility of fitting a parametric lens model to the model ensemble; so far we have only been successful at extracting an Einstein radius.~~

~~The online supplement gives results for all the modelled systems generated for all the lensing candidates.~~

3 IMAGE MORPHOLOGY

~~A modeller's main input to the lens-modelling process is a markup of the candidate lens system, which we call a spaghetti diagram. This is a sketch of the arrival-time surface from a point-like source, with proposed locations of maxima, minima and saddle points, and an implied time-ordering of the images. Such information encodes a starting proposal for the mass distribution. A spaghetti diagram is thus a completely abstract construction, and moreover it refers to a simplified system with a point source. However, spaghetti diagrams are intuitive because they tend to resemble the form of lensed arcs (see Fig. 3 of Ferreras et al. 2008), and of course they are simple to draw, and easy to vary and refine in an open collaborative environment. This makes them very practical for non-professional lens enthusiasts in the citizen-science community. Details and tests are given in Küng et al. (2015).~~

We now discuss the diagnostics that can be taken from the process of drawing the spaghetti diagram, even before detailed mass-modelling takes place. Figure Fig. 2 shows nine examples, each consisting of a cutout of the Space Warps Space Warps image of a lens candidate, marked up with a spaghetti diagram. ~~The volunteers are initially presented a square image with side 82'' (440 pixels) in full size, but they have the ability to zoom in individually. The cutouts presented in Figs. 2 to 5 are rescaled during post-processing, relative to the outermost image.~~

All the examples in Figure shown in Fig. 2 identify five locations: the centre of the main lensing galaxy, which is also a maximum of the arrival time surface (red dots); two minima (blue dots); and two saddle points (green dots and also self-intersections of the curves). Only two (~~SW05 and SW42~~ SW 05 and SW 42) of the nine systems, however, have five distinct features in plausible locations. In the other seven examples, an arc is interpreted as a blend of three or four images. This ~~gives defines~~ the ‘unblended images’ diagnostic. Note that this characterisation could be different if the spaghetti diagram ~~is were~~ different. For example, SW 28 SW 28 has also been modelled with the arc on the right interpreted as a single image, rather than as three images as

shown in the figure; for such a model, ~~the~~ ‘unblended images’ diagnostic would be true.

The second diagnostic ~~is checks~~ whether all images are visible. For example, we see in ~~SW58~~ SW 58 at the top left of Figure Fig. 2 that an image at the second minimum is conjectural and does not correspond to any visible feature.

The third diagnostic ~~is tests~~ whether the lens is ~~fairly~~ isolated, or whether ~~there are other galaxies in the field that probably contribute significantly~~ ~~other galaxies could contribute~~ to the lensing. For this, we do not consider stars or other clearly foreground objects. Additional galaxies contributing to the lensing mass can be marked by the volunteer alongside the spaghetti diagrams. An example can be seen as the grey dot and circle in the cutout with ~~SW57~~ SW 57 at the top right of Figure Fig. 2. Objects marked in this way are modelled as point masses. Other possible contributors to lensing are galaxies or groups that are not in the immediate vicinity of the lensed images, yet massive enough to ~~have an effect exert an influence~~. These are accounted for by allowing a constant but adjustable external shear.

We remark that ~~blended images or missing the lack of expected lensed images, or the presence of blended images~~ or perturbing galaxies do not imply that a given candidate is unlikely to be a lens. ~~They mean~~ This means, rather, that the models are more uncertain and perhaps could be more easily improved by trying further variations in the markup.

The fourth diagnostic is based on the fact that the arrangement of lensed images of a pointlike source through a non-circular gravitational lens depends on the location of the source relative to the long and short axes of the lens. This dependence is quite robust and independent of many other details of the lensing mass distribution. Sources close to being dead-centre behind a lens tend to produce quads; sources at larger transverse distance tend to produce doubles. We denote these as Q and D, respectively, and add a prefix to the Q systems, as follows: we write LQ if the source is inferred as displaced along the long axis of the lens, SQ if displaced along the short axis, IQ if inclined to both axes, CQ if only very little ~~to no inclination or no displacement is evident~~. Although the unlensed source and its location are obviously not seen, the LQ, SQ, IQ and CQ cases correspond to easily-seen image morphologies (see, e.g., Saha & Williams 2003).

- The simplest is the ~~SQ-LQ~~ case: this creates a saddle point and two minima in an arc, with the second saddle point on the other side of the lensing galaxy, ~~and closer to the galaxy than the arc is.~~ ~~SW58 and SW28~~ SW 58 and SW 28 in the upper row of Figure Fig. 2 are typical examples of ~~SQ-LQ~~. If the source were moved outwards along the short axis, the minimum-saddle-minimum set would merge into a single minimum, leaving a D system; this transition is known as a cusp catastrophe.

The middle row of Figure Fig. 2 shows three IQ systems, ~~SW05, SW42 and SW19~~: SW 05, SW 42 and SW 19. This type has a characteristic asymmetry, often with two images close together. If the source were moved outwards, the minimum-saddle pair would merge and mutually cancel, leaving again a D system. This transition is known as a fold catastrophe.

- The lower row of Figure Fig. 2 shows three LQ systems ~~SW09, SW29 and SW02~~: SW 09, SW 29 and SW 02. The failed

model, SW09SW 57, SW29 and SW02, and the failed model SW57 at top right also possibly belonging may also belong to this category. Here the images have a fairly symmetric arrangement with an arc and a counter-image on the other side, but the spaghetti diagram is completely asymmetric. LQ If the source were moved outwards along the long axis, the saddle-minimum-saddle set would merge into a single saddle — another form of cusp catastrophe. SQ can be visually distinguished from SQ from LQ by the relative distances of the arc and the counter-image. For LQ-SQ the arc is closer, for SQ-LQ the counter-image is closer.

Although the CQ systems are often called ‘cross’ or ‘Einstein-cross’ systems; IQ systems are sometimes called ‘folds’, with ‘cusp’ commonly used for both SQ and LQ. The labels ‘short-axis quad’ and so on are not standard in the literature, but the morphological classification they express is familiar to experienced modellers. Hence they can be useful to researchers wishing to apply other modelling methods to the same systems.

4 MASS MODELS

Once a spaghetti diagram has been drawn on a web browser, it is forwarded to a server-side numerical framework, which searches for mass maps consistent with the given image locations, parities and time ordering given by the modeller. The mass maps are made up of mass tiles and are free-form, but are required to be concentrated around the identified lens centre (see Coles et al. 2014, for the precise formulation of the search problem). The modeller can also set various options for the search, such as the number of mass tiles and the extent of the mass map; all options have defaults. Typically, there are ~ 500 mass tiles arranged in a disc, centred on the lensing galaxy and extending to twice the radius of the outermost image. By default, the mass distributed is required to have 180° rotation symmetry, but this option can be unset. Assuming mass distributions can be found (which in practice is usually the case) a statistical ensemble of two-dimensional mass maps is returned. This ensemble, along with derived quantities and uncertainties, makes up one SpaghettiLens model.

The mass will naturally depend on the lens and source redshifts, which are unknown when a lens candidate is first identified. But However, this is not a problem, because a model can be trivially rescaled to use better redshift values, as and when they become available. The mass normalisation of the models is proportional, through the angular critical density, to the factor $d_L d_S d_{LS}^{-1}$, where d_L , d_S and d_{LS} are the usual angular-diameter distances. In the redshift ranges typical of galaxy lensing, the normalisation factor is roughly proportional to the lens redshift, and weakly dependent on the source redshift. This work applies photometric redshifts from the CFHTLS pipeline (Coupon et al. 2009) to the candidate lensing galaxies; the values range from $z = 0.2$ to $z = 1.1$ (see Table 1). As the mass normalisation depends only weakly on source redshift, provided it is larger than to the lens redshift, we assumed all sources to lie at. The source redshifts are assumed as $z = 2$, unless an

unambiguous photometric redshift is available. The lens redshifts entail rather big uncertainties, up to a few tens of percent (see Fig. 5 in Coupon et al. 2009). The lensing masses would be uncertain at the same level. On the other hand, the lensing masses in the sample range from $10^{11} M_\odot$ to $10^{13} M_\odot$; in comparison, the redshift uncertainty is not so important in this preliminary analysis.

The ensemble of mass maps can be post-processed in many different ways. Four different graphical quantities are particularly useful.

Figure Fig. 3 shows the arrival-time surfaces corresponding to the spaghetti diagrams in Figure of Fig. 2. The arrival-time contours look like machine-made elaborations of the input spaghetti diagrams. If the saddle-point contours in the arrival time are qualitatively the same as the curves in the spaghetti diagram (the detailed shape of the spaghetti curves is unimportant), it immediately suggests a successful model. On the other hand, if the arrival-time surface has unexpected minima or saddle points, and especially if the unexpected features are far from identified lens images, that signals a doubtful model. Figure an improbable model. Fig. 4 shows what we call synthetic images, meaning reconstructions of the extended lensed features by fitting for a source. These were generated by a new method, explained in Appendix A1, implemented in during the offline post-processing after the modelling process was complete. The synthetic images provided by SpaghettiLens during the collaborative modelling and discussion were more crude; these those are included in the online supplement.

The arrival-time surface and synthetic image are summarised by one diagnostic, the most important of all: are the lensed features satisfactorily reproduced? This diagnostic remains a judgment call by modellers. A useful quantitative criterion for whether the synthetic image is consistent with the data would need to allow for PSF dependence and unmodelled substructure —otherwise— otherwise all models would be summarily rejected —and it is not clear how to do this rejected, something left for a future implementation in SpaghettiLens.

Figure Fig. 5 shows the projected mass maps of the example systems. Actually sample. In fact, this figure only shows the ensemble-average mass maps, and not the variation within the ensemble, from which uncertainties can be inferred. (The same applies to the arrival-time surfaces and synthetic images in the two previous figures. Uncertainties previous two figures. The uncertainties will be shown in a concise form later, with Figure in Fig. 6.) Figure Fig. 5 makes evident the tiled nature of the mass model. The tiles can be smoothed over by interpolating interpolation, and this was actually done in the mass maps shown online during the modelling process, available in the online version. It is interesting, however, to see note the tiling artifacts, if only as a reminder that the substructure in the mass distribution are is very uncertain, even if some integrated quantities are very well constrained. How the free-form mass maps relate to parameterised lens models is discussed in Appendix A3. Note that the arrival-time surface does not although the mass distribution can have discontinuous jumps, because the modelling numerics uses an analytical integral over square tiles; likewise the lens equation the lens equation and arrival-time surface are continuous.

Figure Fig. 6 shows the enclosed-mass profiles, expressed as the average convergence κ within circles of given projected radius. **This time, uncertainties are included**. Uncertainties are included (see the figure caption for details). Appendix A2 describes the improvements made since our earlier work (Küng et al. 2015), to allow for steeper profiles in the inner regions. The enclosed mass is typically best constrained at the notional Einstein radius, becoming more uncertain at larger and smaller radii.

The mass maps and mass profiles are the basis of a further diagnostic: are the mass distributions plausible? This is also a judgment call made by modellers, but it showed to be a powerful diagnostic, summarizing three aspects. The overall shape is forced to be 180°-rotation symmetric, usually a plausible assumption, but volunteers can deactivate this constraint. The profile slope turned out to be a good indicator of plausible models, as can be seen by contrasting model SW 57 with the rest of the sample: The missing core in Fig. 5 and the flat profile in Fig. 6 disqualify this model. The clumpiness of the mass map is another useful indicator. Flat profile slopes can often be identified directly in the mass map, where the mass tiles form a checkerboard pattern.

5 STELLAR AND HALO MASS ESTIMATES

The stellar masses of the lens galaxies are derived by comparison of the photometric data with stellar M/L estimates from population synthesis models. In principle, a detailed analysis of the spectral energy distribution is needed to derive accurate stellar masses (e.g. Gallazzi & Bell 2009; Taylor et al. 2011). However, estimates to within ≈ 0.3 dex in $\log(M_{\text{stel}}/M_{\odot})$ can be derived with a single colour, preferably tracing a rest-frame colour similar to $U - V$ (see Fig. 1 of Ferreras et al. 2008) – assuming a universal initial mass function (IMF). There is evidence from detailed absorption line strength analysis that massive galaxies can feature a non-standard IMF (e.g. Ferreras et al. 2013). However, these variations – towards a bottom-heavy distribution – are typically found in the cores of massive early-type galaxies (La Barbera et al. 2016). The effect of these variations on the stellar M/L of lensing systems is still rather controversial (Smith et al. 2015; Leier et al. 2016).

In this paper we further simplify the analysis by assuming a relationship between the apparent total magnitude and stellar mass, at the redshift of the lens. For typical stellar-population parameters, the variation of this relation is at most $\Delta \log M_{\text{stel}} \approx 1$ dex. A further possible systematic error is potential systematic can arise from contamination of the light of the lensing galaxy by the lensed background galaxy source. Reducing or eliminating the latter would require detailed fitting of light distributions for each candidate (see Leier et al. 2011), which we have not yet attempted. Nonetheless, because the lensing masses range over two orders of magnitude, it is still interesting to compare with very rough stellar masses them with rough estimates of stellar mass.

We make use of the Bruzual & Charlot (2003) models to derive two functional forms of the stellar mass with respect to SDSS-*i*-band and the *i'*-band magnitudes. The models have solar metallicity, with a Chabrier IMF, and assume two different

age trends: a “young” model, with a constant 500 Myr age at all redshifts, and an “old” model where the age is the oldest one possible at each redshift, adopting a standard Λ CDM model with $H_0 = 70 \text{ km s}^{-1} \text{ Mpc}^{-1}$ and $\Omega_m = 0.3$.

Figure Fig. 7 shows a comparison of stellar and total masses lensing mass in our sample. The comparatively large uncertainty in the stellar mass span of the error bars in stellar mass (horizontal axis) shows the range between the masses derived using the two age trends respectively, and lies between 0.4 and 0.8 dex. It will be improved in future work by using the use of available optical and NIR magnitudes to derive more accurate constraints on the stellar populations.

In addition, we also derive halo masses for the lenses using an abundance-matching formula. This technique matches the distribution function of observed stellar mass in galaxies with that of dark-halo masses in *N*-body simulations to derive to define a simple relation between stellar mass and halo mass. We emphasize that a halo mass from abundance matching should be considered an “average” estimate, and a significant scatter can be expected as galaxies with the same stellar mass can be found in different environments. We refer the reader to Leier et al. (2012) for an assessment of the effect of abundance matching on the derivation of dark matter halo properties in lensing galaxies. We follow the prescription of Moster et al. (2010), namely:

$$\frac{M_{\text{stel}}}{M_{\text{halo}}} = \frac{2C_0}{(M_{\text{halo}}/M_1)^{-\beta} + (M_{\text{halo}}/M_1)^\gamma} \quad C_0 = 0.02820, M_1 = 10^{11.884} M_{\odot} \quad (1)$$

Figure

$$C_0 = 0.02820, \quad M_1 = 10^{11.884} M_{\odot} \\ \beta = 1.057, \quad \gamma = 0.556.$$

Fig. 7 may be compared with Figure Fig. 4 in More et al. (2011).

The comparison of lensing and stellar masses provides us with mass produces the last of our model diagnostics. This is defined as a halo-matching index:

$$\mathcal{H} \equiv \frac{\ln(M/M_{\text{stel}})}{\ln(M_{\text{halo}}/M_{\text{stel}})} \quad (2)$$

that relates the observed lensing to stellar mass, with the global ratio expected if the host halo corresponds to the average value derived by abundance matching. Several cases for \mathcal{H} can be considered:

- $\mathcal{H} < 0$ is unphysical because $M < M_{\text{stel}}$.
- $\mathcal{H} = 0$ is when means the stellar mass exactly accounts for the lensing mass – (i.e. no dark matter affects the lensing model).
- $0 < \mathcal{H} < 1$ is the typical situation, where the lens includes stars and dark matter, but not the full halo.
- $\mathcal{H} = 1$ means that the lens consists of the entire halo.
- $\mathcal{H} > 1$ is in tension with abundance-matching, because the lensing mass exceeds the expected halo mass.

The halo-matching index expresses whether the lensing mass is plausible given the light flux received from the candidate lensing galaxy.

Fig. 7 and Table 1 show that most of the candidates

have stellar and lensing masses typical of massive ellipticals². SW 05 is one of the most massive of all the candidates, corresponding to a galaxy-group mass scale. It is a particularly attractive system for follow-up observations at higher resolution, as it is a large system with clear multiple-image features. Modelling leaves little doubt that it is a lens. SW 04 seems to be even more massive, but the diagnostics leave some doubts about the validity of this model. The two lowest-mass systems, SW 19 and SW 42, are important if they are indeed lenses, as they would be low-mass lenses dominated by dark matter. All the modelled systems have reasonable stellar-mass fractions, except for two cases where the stellar-mass fraction is too low ($\mathcal{H} > 1$); these are SW 42 and SW 57. In the case of SW 57, the model has poor diagnostics and should be discarded. The model for SW 42, on the other hand, is quite convincing – except for the high halo-matching index. If SW 42 turned out not to be a lens, that would support the halo-matching index as an effective criterion to discriminate models.

6 SUMMARY AND CONCLUSIONS

We report on a first set of mass distributions and ~~follow-up~~ diagnostics for the Space Warps lens candidates created with a novel approach that aims to be scalable by ~~orders of magnitudes~~~~orders of magnitude~~ to prepare for the many thousands of lenses the next generation of wide field surveys will yield – (e.g. Euclid, WFIRST).

The Over the past few years, the way of discovering lenses ~~is changing~~ has changed with the introduction of machine learning and citizen science methods, combined with the coverage of ~~huge areas~~~~large areas of the sky~~ by modern surveys. The way ~~mass models~~~~lensing mass models are constructed~~ also needs to change, in order to be prepared for the increasing influx of ~~lenses to be modelled~~. This work is a hybrid of lens candidates. The work in this paper represents a hybrid approach between the classical style – where a small team of experts invest many hours into the creation of a single model, ~~with the approach of citizen science~~, and a citizen science project – where a crowd of amateur volunteers make independent contributions. We ~~The authors of this paper~~ are a collaboration of professionals and experienced citizen-science volunteers, aiming to create early-stage lens models as soon as a lens candidate is found.

To assist volunteer modellers assessing their assist volunteers in constraining lensing models, we introduce a set of diagnostics allowing the qualification of the lenses and the generated models and present them alongside the generated models that help assess the validity of the models. At a later stage, we encourage modellers to apply those diagnostics themselves to get a preliminary ~~as~~ feedback on the plausibility of their models, assumptions, and to suggest additional diagnostics.

The diagnostics (i) – (iv) (see Section 2) turned out to be useful measures of the difficulty in modelling a system, but they did not constitute necessary conditions for a promising model. They can help select systems to introduce novice volunteers to the modelling process. In contrast,

diagnostics (v) and (vi) can be considered as necessary criteria for a good model. Volunteers employed those ones to evaluate their models, and turned out to be easy enough to grasp by new volunteers. The halo-matching index diagnostic (vii, \mathcal{H}), is an interesting criterion that might be useful for the modellers, but needs further investigation.

Table 1 is a summary of our results. It characterises each modelled system with seven diagnostics, indicating (a) the image morphology and how clear or indistinct it is, (b) whether the mass map and synthetic lensed image appear to be plausible, and (c) how the model mass compares with the estimated stellar and full-halo masses. Missing entries are due to photometry data not being available~~unavailable imaging data~~, whereas missing rows are due to models not having been created for this particular candidate.

Figure 7 is another summary. It shows most of the candidates having stellar and total mass typical of massive ellipticals. SW05 is one of the most massive of all the candidates, with a mass of galaxy-group scale. It is a particularly attractive system for follow-up observations at higher resolution, as it is a large system with clear multiple image features, and modelling leaves little doubt that it is a lens. SW04 seems to be even more massive, but the diagnostics leave some doubts about this model. The two lowest-mass systems, SW19 and SW42, are important if they are indeed lenses, as they would be low-mass lenses dominated by dark matter. All the modelled systems have reasonable stellar-mass fractions, except for two cases where the stellar-mass fraction is too low (halo-matching index > 1); these are SW42 and SW57. In the case of SW57, the model has poor diagnostics and should be discounted. The model for SW42, on the other hand, is quite convincing – except for the high halo-matching index. If SW42 turns out not to be a lens, that would support the halo matching index as an effective criterion for filtering models.

The trend in Fig. 7, that where higher-mass galaxies get progressively more dark-matter dominated, is expected, ~~e.g. see Ferreras et al. (2005)~~, as is the span of about one order of magnitude for the stellar mass and the two ~~order of magnitudes for the total orders of magnitude in lensing~~ mass. With future data, it ~~would~~ ~~will~~ be interesting to compare the enclosed stellar and ~~total lensing~~ mass as a function of radius, going from the star-dominated inner regions to the outer dark halos. Leier et al. (2011) illustrate this behaviour in their Fig. 5, but the present sample could go an order of magnitude higher in mass.

The quick creation of many models for the Space Warps candidates successfully showed that a subset of citizen scientists are interested in being involved in more challenging tasks that take some time to learn. A next step involves recruiting more lensing enthusiasts, as soon as the next round of Space Warps is started. In the meantime, the improvements shown in the Appendix ~~have to be integrated into regular~~ will be integrated in the standard version of SpaghettiLens~~usage~~. Additionally, photometric fitting could be integrated into SpaghettiLens. This would allow experienced citizen scientists to generate photometric redshifts and stellar masses, and thus generate preliminary dark-matter maps as soon as a lens-candidate is identified.

² Exact values can be found in the online version of Table 1

REFERENCES

- Bruderer C., Read J. I., Coles J. P., Leier D., Falco E. E., Ferreras I., Saha P., 2016, *MNRAS*, **456**, 870
- Bruzual G., Charlot S., 2003, *MNRAS*, **344**, 1000
- Coles J. P., Read J. I., Saha P., 2014, *MNRAS*, **445**, 2181
- Coupon J., et al., 2009, *A&A*, **500**, 981
- Cuillandre J.-C. J., et al., 2012, in Observatory Operations: Strategies, Processes, and Systems IV. p. 84480M, doi:10.1117/12.925584
- Erben T., et al., 2013, *MNRAS*, **433**, 2545
- Ferreras I., Saha P., Williams L. L. R., 2005, *ApJ*, **623**, L5
- Ferreras I., Saha P., Burles S., 2008, *MNRAS*, **383**, 857
- Ferreras I., La Barbera F., de la Rosa I. G., Vazdekis A., de Carvalho R. R., Falcón-Barroso J., Ricciardelli E., 2013, *MNRAS*, **429**, L15
- Gallazzi A., Bell E. F., 2009, *ApJS*, **185**, 253
- Gavazzi R., Marshall P. J., Treu T., Sonnenfeld A., 2014, *ApJ*, **785**, 144
- Heymans C., et al., 2012, *MNRAS*, **427**, 146
- Hezaveh Y. D., Perreault Levasseur L., Marshall P. J., 2017, ArXiv:1708.08842,
- Keeton C. R., 2001, preprint, ([arXiv:astro-ph/0102341](https://arxiv.org/abs/astro-ph/0102341))
- Koopmans L. V. E., et al., 2009, *ApJ*, **703**, L51
- Küng R., et al., 2015, *MNRAS*, **447**, 2170
- La Barbera F., Vazdekis A., Ferreras I., Pasquali A., Cappellari M., Martín-Navarro I., Schönebeck F., Falcón-Barroso J., 2016, *MNRAS*, **457**, 1468
- Lanusse F., Ma Q., Li N., Collett T. E., Li C.-L., Ravankhah S., Mandelbaum R., Poczos B., 2017, preprint, ([arXiv:1703.02642](https://arxiv.org/abs/1703.02642))
- Leier D., Ferreras I., Saha P., Falco E. E., 2011, *ApJ*, **740**, 97
- Leier D., Ferreras I., Saha P., 2012, *MNRAS*, **424**, 104
- Leier D., Ferreras I., Saha P., Charlot S., Bruzual G., La Barbera F., 2016, *MNRAS*, **459**, 3677
- Marshall P. J., et al., 2016, *MNRAS*, **455**, 1171
- Maturi M., Mizera S., Seidel G., 2014, *A&A*, **567**, A111
- McGaugh S. S., Lelli F., Schombert J. M., 2016, *Physical Review Letters*, **117**, 201101
- More A., Jahnke K., More S., Gallazzi A., Bell E. F., Barden M., Häußler B., 2011, *ApJ*, **734**, 69
- More A., Cabanac R., More S., Alard C., Limousin M., Kneib J.-P., Gavazzi R., Motta V., 2012, *ApJ*, **749**, 38
- More A., et al., 2016, *MNRAS*, **455**, 1191
- Moster B. P., Somerville R. S., Maulbetsch C., van den Bosch F. C., Macciò A. V., Naab T., Oser L., 2010, *ApJ*, **710**, 903
- Nightingale J., Dye S., Massey R., 2017, ArXiv:1708.07377,
- Paraficz D., et al., 2016, *A&A*, **592**, A75
- Saha P., Williams L. L. R., 2003, *AJ*, **125**, 2769
- Saxton C. J., Ferreras I., 2010, *MNRAS*, **405**, 77
- Schive H.-Y., Chiueh T., Broadhurst T., Huang K.-W., 2016, *ApJ*, **818**, 89
- Silk J., Mamon G. A., 2012, *Research in Astronomy and Astrophysics*, **12**, 917
- Smith R. J., Lucey J. R., Conroy C., 2015, *MNRAS*, **449**, 3441
- Sonnenfeld A., et al., 2017, preprint, ([arXiv:1704.01585](https://arxiv.org/abs/1704.01585))
- Springel V., et al., 2005, *Nature*, **435**, 629
- Taylor E. N., et al., 2011, *MNRAS*, **418**, 1587

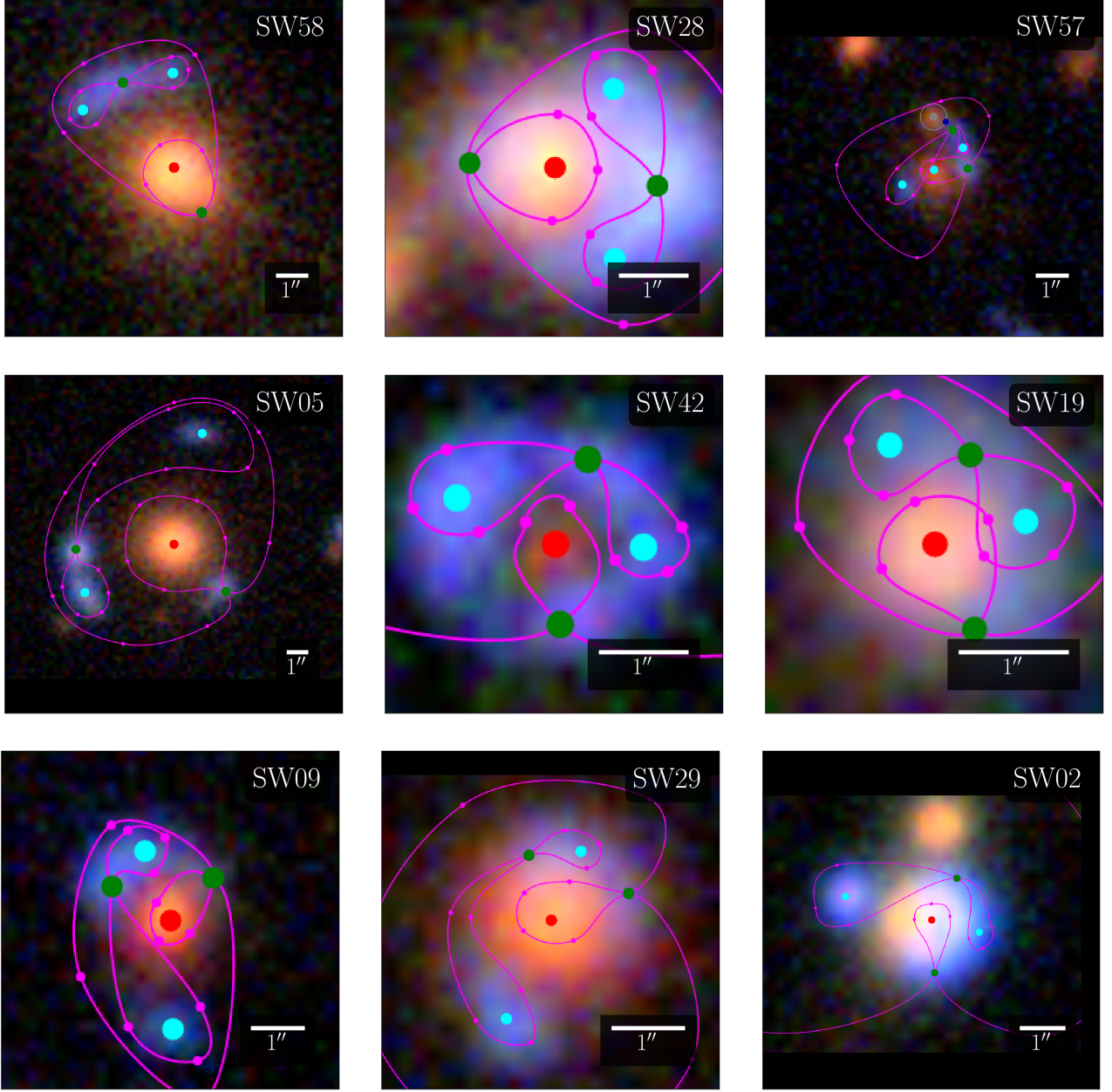


Figure 2. Nine of the lens candidates marked up with spaghetti diagrams. Red, blue and green dots are proposed locations for maxima, minima and saddle points of the arrival time respectively. The curves help guide the placement of the dots, but their precise appearance has no significance. This images are screenshots from the SpaghettiLens user interface, which applies interpolation to background images. The scaling is adjusted to fit the other images. This selection includes the best-modelled systems, but also one case (SW57-SW 57 at upper right) of unsuccessful modelling. Since the modelling process is collaborative among the volunteers, with anyone welcome to contribute new models or modify existing ones, there are variant spaghetti diagrams for all the modelled systems. The online supplement displays all the models presented for discussion during this work.

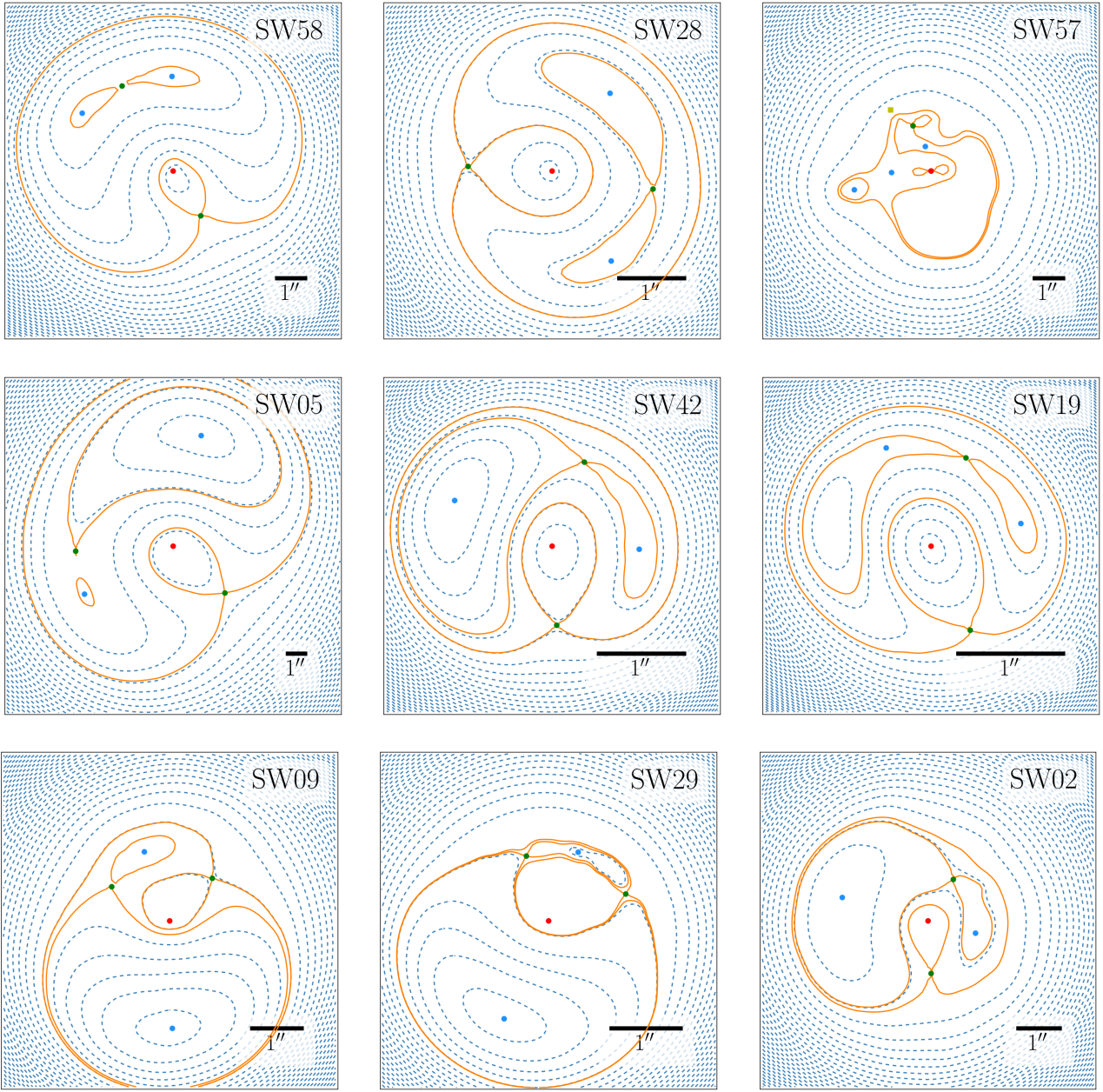


Figure 3. Arrival-time surfaces for models of the systems from Figure 2. The registration differs slightly from Figure 2, but the coloured dots represent exactly the sky positions specified in the earlier figure. The orange contours only qualitatively resemble the earlier pink curves, as they are now precise saddle-point contours from lens models.

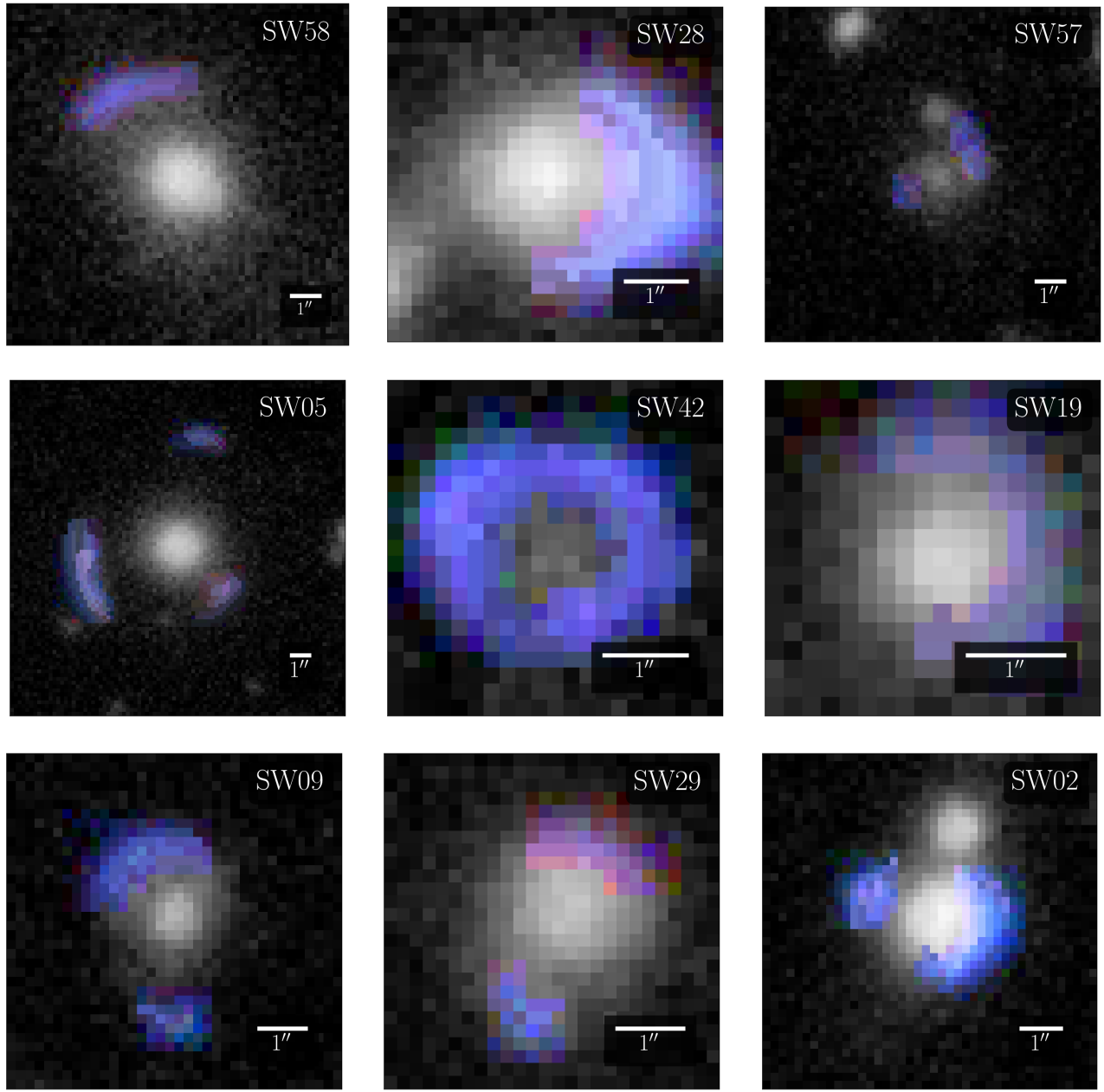


Figure 4. Synthetic images of the systems from Figure 2, derived from the lens models. The reconstructed lensed features keep the Space Warps false-colour scheme from Figures 2. The rest has been changed to black-and-white.

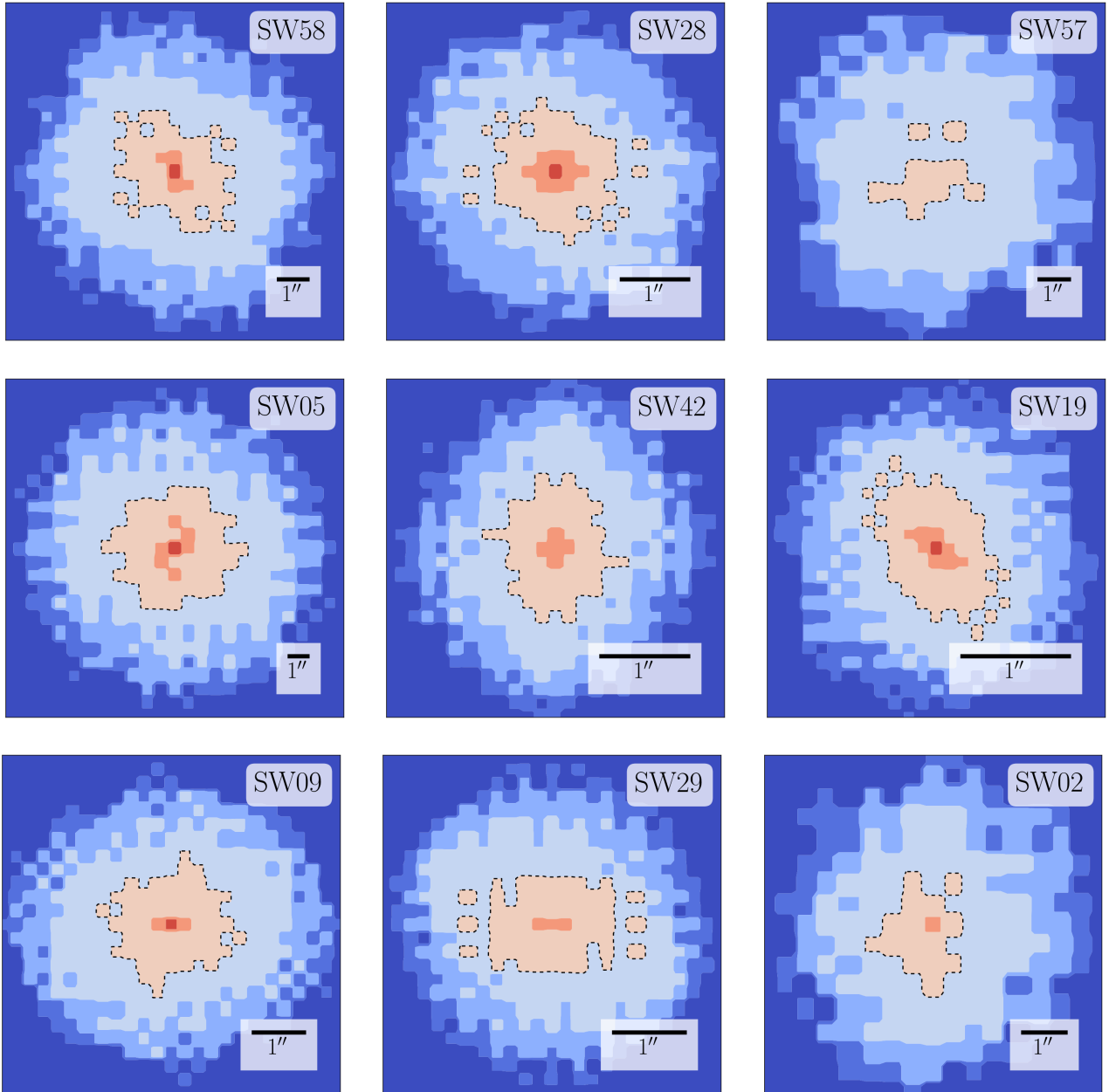


Figure 5. Ensemble-average mass distribution κ for which the results Figures 3–4 were derived. The dashed curves denote $\kappa = 1$. Most of the mass maps have a 180° -rotation symmetry, which is imposed by default. For **SW02**–SW 02 and **SW57**–SW 57, where the lensing mass is clearly asymmetric, the modeller chose to turn off the symmetry.

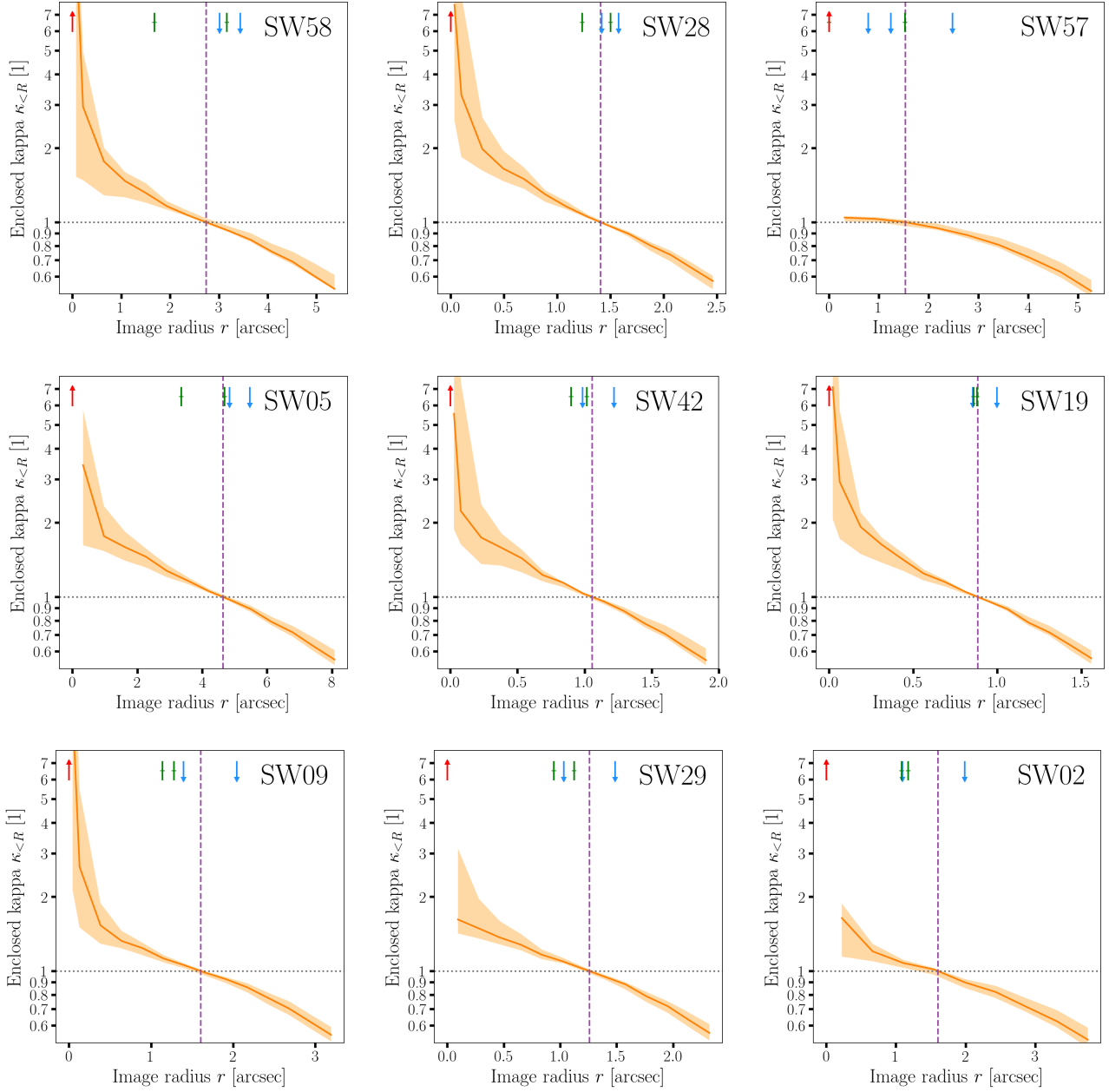


Figure 6. Cumulative circular-averages of the mass maps from Figure 5, with uncertainties. More precisely, we show the enclosed mass within a given projected radius, expressed as the mean κ with a given number of arcsec from the centre of the lensing galaxy. The orange bands refer to the full ensemble of mass maps for the models, while the red curves show the ensemble averages. The dashed vertical line indicates the notional Einstein radius, or where the mean enclosed κ is unity. The short vertical arrows marks the positions of the images (maxima, saddle points and minima).

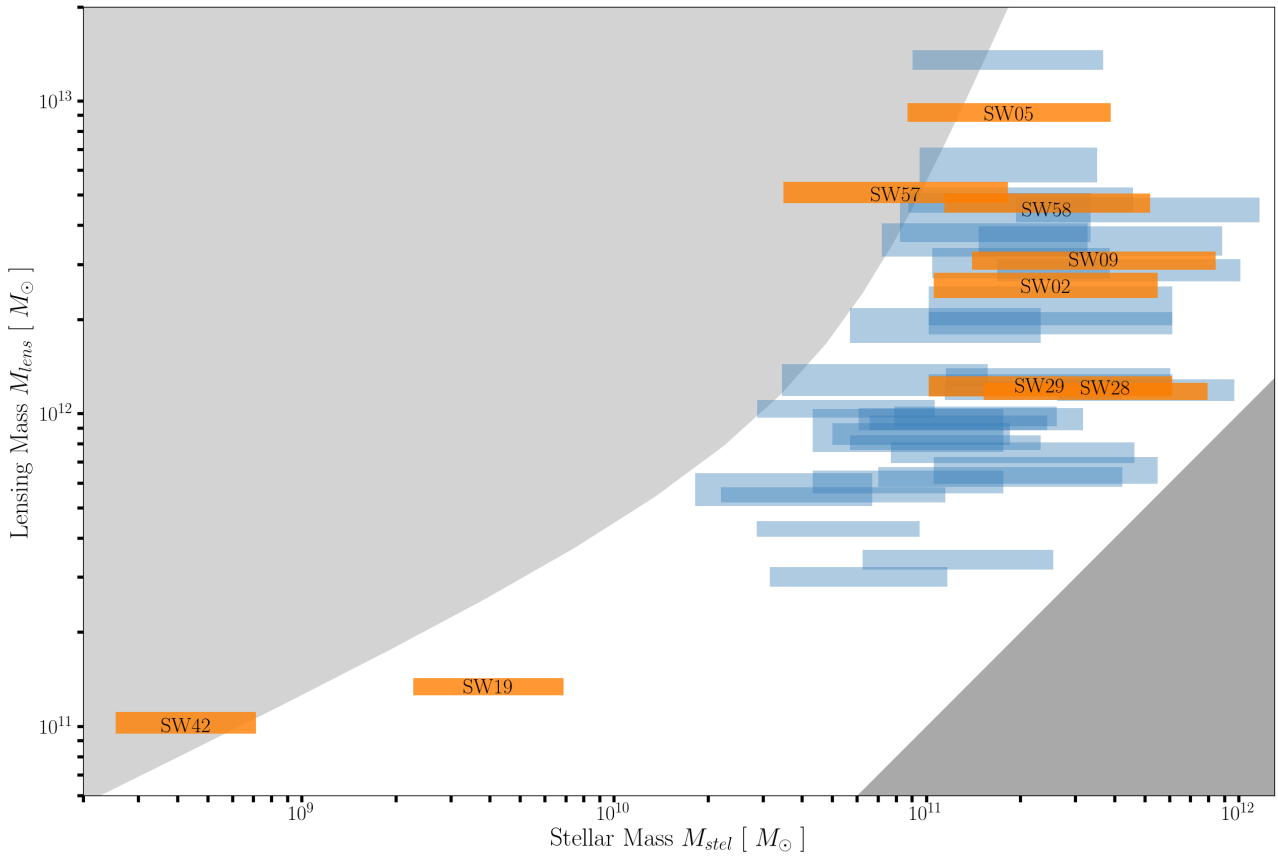


Figure 7. Total mass in the model against the estimated stellar mass, alongside the values for the whole sample. (The labelled orange bars are the systems shown in detail in Figures 2–6.) The horizontal extent of each bar indicates the extreme cases of a young (0.5 Gyr-old) stellar population and the oldest possible population at the given redshift. The vertical extent indicates the spread of masses in the lens-model ensemble. The lower-right shaded region is unphysical according to the stellar-population models, because it gives $M < M_{\text{stel}}$. The upper-left shaded region is unphysical according to abundance matching (see Section 5) because it gives $M > M_{\text{halo}}$. That is to say, the unshaded region is $0 < \mathcal{H} < 1$.

Table 1. Diagnostics of [a-the](#) selected [model-models](#) for each [Space Warps](#) Space Warps candidate (see Section 6).

SWID	ZooID	CFHTLS Name	z_{lens}	unblended images	all images discernible	isolated lens	image morphology	synthetic image reasonable	mass map reasonable	$\log_{10} \frac{M_{\text{stel}}}{M_{\odot}}$	$\log_{10} \frac{M_{\text{lens}}}{M_{\odot}}$	halo-matching
SW01 -SW 01	ASW0004dv8 -ASW000 4dv8	J022409.5-105807	—	✗	✗	✗	SQ-LQ	✓	✓	—	—	—
SW02 -SW 02	ASW000619d -ASW000 619d	J140522.2+574333	0.7	✗	✓	✗	LQ-SQ	✓	✓	11.4	12.4	0.47
SW03 -SW 03	ASW0006mea -ASW000 6mea	J142603.2+511421	—	✓	✗	✗	D	✓	✓	—	—	—
SW04 -SW 04	ASW0009ejs -ASW000 9cjs	J142934.2+562541	0.5	✓	✗	✗	EQ-D	✗	✓	11.3	13.1	0.93
SW05 -SW 05	ASW0007k4r -ASW000 7k4r	J143454.4+522850	0.58	✓	✓	✓	IQ	✓	✓	11.3	13.0	0.83
SW06 -SW 06	ASW0008swn -ASW000 8swn	J143627.9+563832	0.5	✗	✓	✓	LQ-SQ	✓	✗	11.1	11.9	0.46
SW07 -SW 07	ASW0007e08 -ASW000 7e08	J220256.8+023432	—	✓	✓	✗	D	✓	✓	—	—	—
SW08 -SW 08	ASW0009ed -ASW000 9ned	J020648.0-065639	0.8	✓	✓	✗	D	✓	✓	11.4	12.3	0.40
SW09 -SW 09	ASW0002asp -ASW000 2asp	J020832.1-043315	1.0	✗	✓	✓	SQ	✓	✓	11.5	12.5	0.40
SW10 -SW 10	ASW0002bmc -ASW000 2bmc	J020848.2-042427	0.8	✓	✗	✓	D	✗	✗	11.3	11.9	0.29
SW11 -SW 11	ASW0002qtn -ASW000 2qtn	J020849.8-050429	0.8	✗	✓	✗	LQ	✓	✓	11.2	11.8	0.29
SW12 -SW 12	ASW0003wsu -ASW000 3wsu	J022406.1-062846	0.4	✓	✓	✗	D	✓	✓	10.8	11.5	0.44
SW13 -SW 13	ASW00047ae -ASW000 47ae	J022805.6-051733	0.4	✗	✗	✗	LQ-SQ	✗	✗	11.1	11.9	0.46
SW14 -SW 14	ASW0004xjk -ASW000 4xjk	J023123.2-082535	—	✗	✗	✗	SQ	✗	✓	—	—	—
SW15 -SW 15	ASW0004nan -ASW000 4nan	J084841.0-045237	0.3	✗	✓	✗	LQ-CQ	✓	✓	10.7	11.6	0.59
SW16 -SW 16	ASW0009bp2 -ASW000 9bp2	J140030.2+574437	0.4	✗	✗	✓	D	✗	✓	11.3	12.1	0.34
SW17 -SW 17	ASW0005rn8 -ASW000 5rn8	J140622.9+520942	0.7	✓	✗	✗	D	✗	✓	11.1	12.0	0.44
SW18 -SW 18	ASW0007hu2 -ASW000 7hu2	J143658.1+533807	0.7	✓	✗	✓	D	✗	✗	11.4	12.1	0.31
SW19 -SW 19	ASW0001ld7 -ASW000 1ld7	J020642.0-095157	0.2	✗	✓	✗	IQ	✗	✓	9.6	11.1	0.84
SW20 -SW 20	ASW0002dx7 -ASW000 2dx7	J021221.1-105251	0.3	✓	✓	✓	IQ-D	✗	✓	11.2	12.0	0.44
SW21 -SW 21	ASW0004m3x -ASW000 4m3x	J022533.3-053204	0.5	✓	✗	✗	D	✗	✓	11.1	11.5	0.24
SW22 -SW 22	ASW0009ab8 -ASW000 9ab8	J022716.4-105602	0.4	✗	✗	✗	D	✗	✓	11.7	12.1	0.15
SW23 -SW 23	ASW0003r61 -ASW000 3r61	J023008.6-054038	0.6	✗	✓	✗	SQ-LQ	✗	✓	11.2	12.6	0.71
SW24 -SW 24	ASW0005osk -ASW000 5osk	J023315.2-042243	0.7	✗	✓	✗	LQ-D	✓	✓	11.4	11.8	0.19
SW25 -SW 25	ASW0007mq -ASW000 07mq	J090308.2-043252	—	✗	✗	✓	D	✗	✓	—	—	—
SW26 -SW 26	ASW0005ma2 -ASW000 5ma2	J135755.8+571722	0.8	✓	✗	✓	D	✗	✗	11.4	12.3	0.43
SW27 -SW 27	ASW0006jh5 -ASW000 6jh5	J141432.9+534004	0.7	✗	✗	✗	LQ	✗	✓	10.7	11.7	0.67
SW28 -SW 28	ASW0007xrs -ASW000 7xrs	J143055.9+572431	0.7	✗	✓	✗	LQ	✓	✓	11.5	12.1	0.23
SW29 -SW 29	ASW0008qsm -ASW000 8qsm	J143838.1+572647	0.8	✗	✓	✓	SQ	✓	✓	11.4	12.1	0.31
SW30 -SW 30	ASW0002p8y -ASW000 2p8y	J021057.9-084450	—	✓	✗	✗	IQ	✗	✗	—	—	—
SW31 -SW 31	ASW00021r0 -ASW000 21r0	J021514.6-092440	0.7	✗	✓	✗	LQ	✓	✓	11.3	12.7	0.65
SW32 -SW 32	ASW0004iye -ASW000 4iye	J022359.8-083651	—	✗	✓	✗	IQ	✓	✓	—	—	—
SW33 -SW 33	ASW0003s0m -ASW000 3s0m	J022745.2-062518	0.6	✓	✓	✗	D	✗	✓	10.9	12.1	0.77
SW34 -SW 34	ASW00051ld -ASW000 51ld	J023453.5-093032	0.5	✗	✗	✓	D	✗	✓	10.9	11.9	0.59
SW35 -SW 35	ASW0004wgd -ASW000 4wgd	J084833.2-044051	0.8	✗	✓	✗	LQ	✓	✓	11.4	12.1	0.32
SW36 -SW 36	ASW000096t -ASW000 096t	J090248.4-010232	0.4	✓	✓	✓	D	✗	✓	11.0	12.0	0.56
SW37 -SW 37	ASW00086xq -ASW000 86xq	J143100.2+564603	—	✗	✗	✓	SQ	✓	✓	—	—	—
SW38 -SW 38	ASW0009ep0 -ASW000 9cp0	J143353.6+542310	0.8	✗	✓	✓	LQ	✓	✓	11.6	12.6	0.42
SW39 -SW 39	ASW0005qiz -ASW000 5qiz	J220215.2+012124	—	—	—	—	—	—	—	—	—	—
SW40 -SW 40	ASW0008wmr -ASW000 8wmr	J221306.1+014708	—	✗	✓	✓	SQ	✓	✓	—	—	—
SW41 -SW 41	ASW0008xbu -ASW000 8xbu	J221519.7+005758	0.4	✓	✗	✓	IQ	✓	✓	10.5	11.8	0.80
SW42 -SW 42	ASW00096rm -ASW000 96rm	J221716.5+015826	0.1	✓	✓	✓	IQ	✓	✓	8.6	11.0	1.04
SW43 -SW 43	ASW0001c3j -ASW000 1c3j	J020810.7-040220	1.0	✗	✗	✗	IQ-SQ	✗	✓	11.6	12.4	0.34
SW44 -SW 44	ASW0002k40 -ASW000 2k40	J021021.5-093415	0.4	✓	✓	✗	D-LQ	✓	✓	11.3	12.8	0.76
SW45 -SW 45	ASW00024id -ASW000 24id	J021225.2-085211	0.8	✗	✓	✓	CQ	✗	✓	11.7	12.6	0.37
SW46 -SW 46	ASW00024qe -ASW000 24qe	J021317.6-084819	0.5	✓	✓	✗	D	✓	✓	10.9	11.8	0.49
SW47 -SW 47	ASW0003r6e -ASW000 3r6e	J022843.0-063316	0.5	✓	✗	✓	D	✗	✓	11.2	12.6	0.71
SW48 -SW 48	ASW0000g95 -ASW000 0g95	J090219.0-053923	—	✓	✗	✓	D	✓	✓	—	—	—
SW49 -SW 49	ASW00007ls -ASW000 07ls	J090319.4-040146	—	✗	✓	✓	D	✓	✓	—	—	—
SW50 -SW 50	ASW0008a0 -ASW000 08a0	J090333.2-005829	—	✓	✗	✓	LQ	✓	✓	—	—	—
SW51 -SW 51	ASW0006e0e -ASW000 6e0e	J135724.8+561614	—	✓	✓	✓	D	✗	✓	—	—	—
SW52 -SW 52	ASW0006a07 -ASW000 6a07	J140027.9+541028	—	✓	✗	✓	LQ-SQ	✓	✓	—	—	—
SW53 -SW 53	ASW0007v1 -ASW000 7v1	J141518.9+513915	0.4	✓	✗	✓	D	✗	✓	11.3	12.5	0.56
SW54 -SW 54	ASW0007sez -ASW000 7sez	J142620.8+561356	0.5	✗	✓	✗	CQ	✓	✓	11.1	12.3	0.68
SW55 -SW 55	ASW0007t5y -ASW000 7t5y	J142652.8+560001	—	✗	✓	✓	CQ	✓	✗	—	—	—
SW56 -SW 56	ASW0007pga -ASW000 7pga	J142843.5+543713	0.4	✓	✗	✓	D	✗	✗	10.7	12.0	0.80
SW57 -SW 57	ASW0008pag -ASW000 8pag	J143631.5+571131	0.7	✗	✓	✗	LQ-SQ	✗	✗	10.9	12.7	1.08
SW58 -SW 58	ASW0007iwp -ASW000 7iwp	J143651.6+530705	0.6	✗	✗	✓	SQ-LQ	✓	✓	11.4	12.6	0.58
SW59 -SW 59	ASW00085ep -ASW000 85cp	J143950.6+544606	—	✓	✗	✓	D	✓	✓	—	—	—

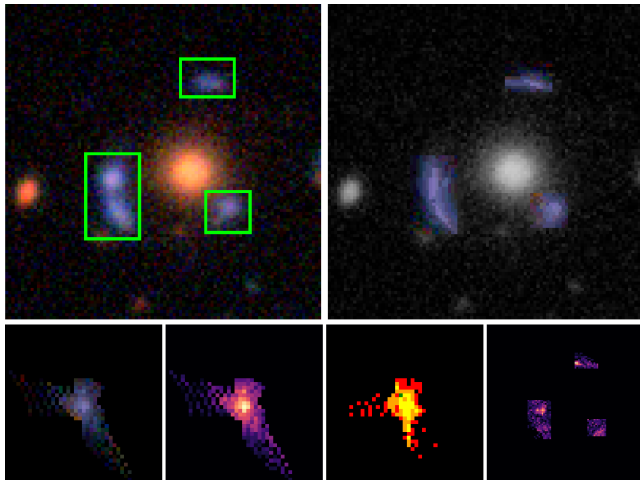


Figure A1. Synthetic lensed image with source-profile fitting in SW05 (J143454.4+522850). Top-left: original image, with areas containing lensed images enclosed within green frames. Top-right: synthetic image (coloured arcs) with lensing galaxy and unrelated objects in greyscale. Bottom from left to right: reconstructed source in colour, intensity (greyscale), count of lens plane pixels per source plane pixel, residual of original image to synthetic image.

APPENDIX A: DEVELOPMENTS IN SPAGHETTILENS

A1 Improved synthetic images

The mass maps produced by the current implementation of SpaghettiLens are based on images of point-like features. No information about extended images is used, except in so far as they help the user identify images of point-like features. The synthetic images offered to users are rudimentary, corresponding to conical light profiles (*that is, i.e.* circular light profiles with brightness decreasing linearly with radius).

We have now developed a prototype to improve the generation of synthetic images, *as illustrated in Fig. A1*. *Figure A1 illustrates First, areas Areas* containing lensed images are selected (green frames in the figure). The selected areas should be as free as possible from *of light from other sources, including the lensing galaxy or from extraneous objects*. Pixels within the selected areas are mapped to a grid on the source plane, using bending angles given by the mass model. The mapping from lens-plane pixels to source-plane grid cells is many-to-one, because of image multiplicity and magnification. The brightness of each source-plane pixel is set to the mean of all the lens-plane pixels *mapping mapped* to it. Finally, the mapping is run back to the lens plane. The result is a synthetic image. In effect, one is reconstructing a source-plane brightness map by least-squares.

The procedure is not yet implemented in SpaghettiLens but can be applied *in during* post-processing. The new synthetic images could be used to improve the mass reconstruction, by *weighting weighing* the ensemble of maps according to how good the synthetic images are, *but we have not attempted to do so as yet*.

A2 Sub-sampling of *the* central region

The models of simulated lenses in Küng et al. (2015) showed a tendency to produce density profiles which were too shallow. *Allowing smaller, resulting typically in overestimates of the Einstein radius. Allowing some extra mass tiles in the central region, thus allowing the mass profile to rise more steeply near the centre, was suggested as a possible cure.*

Figure Fig. A2 shows an experiment with smaller mass tiles in the inner region. Replacing the very central mass tile with 9 smaller tiles allows for steeper central profiles. Doing the same for the 25 innermost mass tiles allows for still even steeper central profiles, eliminating the systematic shallowness. This is, however, still not shallow profiles. However, it does not provide a completely satisfactory solution, because (a) it increases the number of mass tiles by 40% and significantly increases the computational time, and (b) the square boundary between area areas with different tile sizes is rather undesirable. The main modelling work in this paper was, however, done before the experiments with smaller mass tiles was complete. Some of the models presented in this paper apply the intermediate option (corresponding to the middle panel in Figure Fig. A2) while others use the old system. The results in this paper, however, mainly concern We note this paper mainly concerns the enclosed mass in the outer regions, so shallowness in the central region should be inconsequential not be an issue.

A3 Parameterisation Parametrization of pixel models

In order to fit the set of pixelated models to a single parameterised parametrized model, a program programme was written that took a parameterised parametrized function and subtracted from it the mean and the principal components (PCs) of the data, *which were calculated using classical Principal Component Analysis*. This created the residuals residual function. The number of components used principal components in the analysis was varied, to test how this affected the output, *and it*. It was found that *using 5 principal components tended to give PCs gave* a reasonable approximation. A masking function was added *which selected selecting* only the data points that fell inside the image of the lens, and the principal components PCs were clipped in order to keep the values inside the region of the ensemble of models. Any value higher than the clip was set to be the clip value. This was chosen to be -2.5 *as because*, assuming that the data follows a Gaussian error distribution, almost all the values for the variance should lie between 2 and 3 standard deviations from the mean. Minimising the residuals function produces the set of parameters that fit the parameterised parametrized function to the original pixelated ensemble most closely. A least squares fit was used to perform this minimisation. The parameterised parametrized model function was obtained from the gravitational potential of an isothermal ellipsoid mass distribution (Keeton 2001). This model is frequently used to describe gravitational lenses *as it tends to fit well with, giving good fits to the* observations. The isothermal ellipsoid model outputs three useful parameters: the radius of the Einstein ring, the ellipticity of the model and the angle of the ellipticity from the vertical, giving the orientation of the galaxy. By applying this model

to simulated lenses for which the values of these parameters were already known, it was possible to gain an estimate of the projected assess the accuracy of the results methodology, before applying the model to the candidate lensing galaxies.

Preliminary results on the recovery of Einstein radii are shown in Figure Fig. A3.

This paper has been typeset from a T_EX/L_AT_EX file prepared by the author.

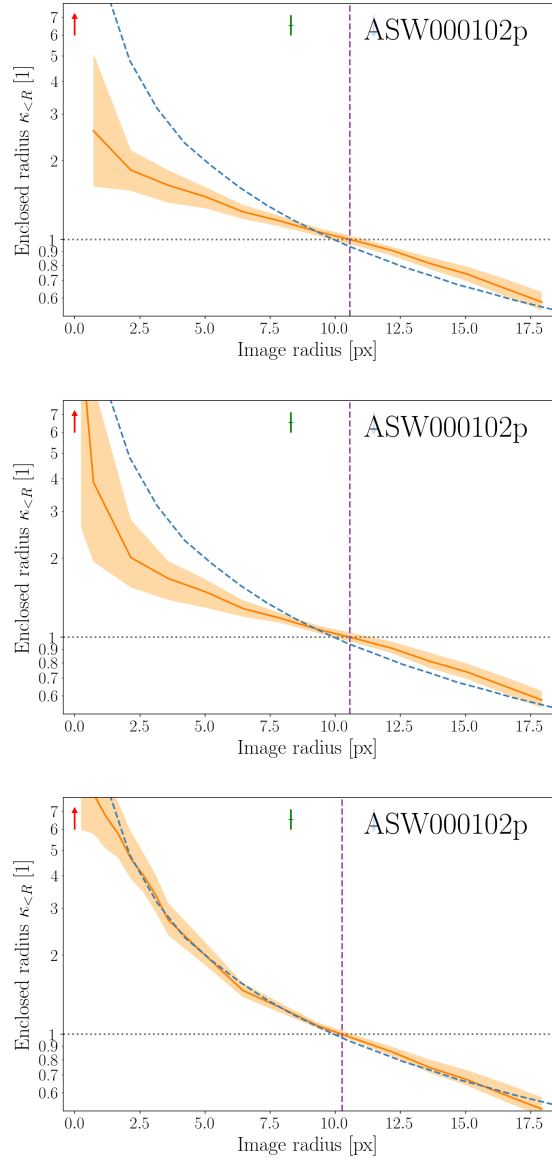


Figure A2. Model improvement resulting from using the use of smaller mass tiles in the inner region of the mass model. Shown here are the average enclosed κ within a given projected radius, for three different reconstructions of a simulated lens (sim) from Space Warps. In each panel, the dashed blue curve is the correct answer. The orange band represents the statistical ensemble from SpaghettiLens, the orange line being shows the ensemble mean. Locations of images (maximum, saddle point, minimum) are marked with vertical arrows. Crossing the horizontal The radial value at $\kappa = 1$ line is the effective Einstein radius r_E . The upper panel is taken from Küng et al. (2015). The middle panel is the result when the innermost mass tile is replaced by 9 smaller tiles. The lower panel results from replacing each of the innermost 5 by $\times 5$ tiles each with 9 smaller tiles each.

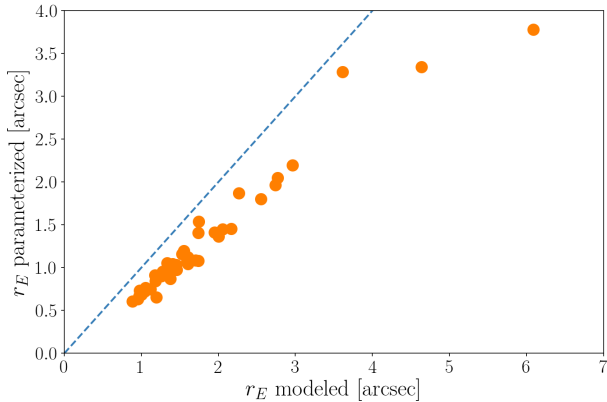


Figure A3. Comparison of Einstein radii r_E obtained from mass tiles directly to those obtained from a parameterized model to test the performance of the parametrisation algorithm. The parameterized model was generated using principle component analysis on the ensemble of models. The blue dashed line represents a perfect recovery of r_E .